remote sensing

MDPI

Article

Application of Ground-Penetrating Radar with the Logging Data Constraint in the Detection of Fractured Rock Mass in Dazu Rock Carvings, Chongqing, China

Wenxing Yuan [1], Sixin Liu [1,*], Qiancheng Zhao [1], Li Deng [1], Qi Lu [1], Lei Pan [2] and Zhilian Li [1]

[1] College of Geo-Exploration Science and Technology, Jilin University, 938 Ximinzhu Street, Changchun 130026, China
[2] CGE (Chongqing) Geological Instrument Co., Ltd., Chongqing 400032, China
* Correspondence: liusixin@jlu.edu.cn

Abstract: Geologic interpretation results from conventional ground-penetrating radar (GPR) detection methods tend to have a certain degree of uncertainty. In order to improve the reliability of ground-penetrating radars in the detection of rock mass fissures in grottoes, this study proposes a ground-penetrating radar detection method with the logging data constraint, which is applied to detect the fractured rock mass in the Baodingshan Scenic Area of Dazu Rock Carvings, Chongqing, China. First, conventional logging and borehole televiewer data were compared and verified, yielding detailed lithological and wellbore fissure information. Next, electromagnetic wave velocity was calibrated using GPR profile and the depth of the stratigraphic interface determined by borehole data. Utilizing this calibrated velocity, we are able to accurately calculate the depth values of anomalies in GPR interpretation profiles. Subsequently, we compared the preliminary GPR interpretation profile with the borehole televiewer images. After eliminating false anomalies caused by interference, we obtained more reliable location information for detection targets such as fissures, fracture zones, and weak interlayers. The results of fissure detection in the Dazu Rock Carvings indicate that the detection results of ground-penetrating radar are verified and supplemented under the constraints of stratigraphic and well-wall fissure information obtained by logging. This effectively mitigates the influence of multiplicity and false anomalies of GPR detection on interpretation results. GPR with the logging data constraint enhances the accuracy of the fissure detection results, providing novel technical means for the protection and restoration of grotto relics.

Keywords: Dazu Rock Carvings; GPR; conventional logging; borehole televiewer; rock mass fissures

Citation: Yuan, W.; Liu, S.; Zhao, Q.; Deng, L.; Lu, Q.; Pan, L.; Li, Z. Application of Ground-Penetrating Radar with the Logging Data Constraint in the Detection of Fractured Rock Mass in Dazu Rock Carvings, Chongqing, China. *Remote Sens.* **2023**, *15*, 4452. https://doi.org/10.3390/rs15184452

Academic Editor: Massimiliano Pieraccini

Received: 24 July 2023
Revised: 30 August 2023
Accepted: 8 September 2023
Published: 10 September 2023

1. Introduction

Grottoes are ancient artworks created by excavating rocks, and they possess significant historical, cultural, artistic and scientific value [1]. However, grotto cultural relics are susceptible to various diseases caused by long-term natural weathering and human activities. Among them, rock mass fissure is recognized as one of the most severe diseases [2]. Non-destructive detection technology can systematically examine the interior of the grotto rock mass and promptly identify fracture zones. This technology can provide valuable reference materials for the subsequent restoration of the grotto rock mass. Consequently, this type of detection technology is crucial for the preservation and research of grotto cultural relics.

Various geophysical methods have been applied for fissure detection, such as Ground-Penetrating Radar (GPR) [3,4], electrical prospecting [5,6], electromagnetic prospecting [7], Nuclear Magnetic Resonance (NMR) [8,9], acoustic exploration [10,11], CT scanning [12,13], and comprehensive logging [14,15]. However, these methods are rarely applied to detect fissures in rock cultural relics; they are mostly used for fissures in reservoir rock mass and hydrogeological related fissures [16–18].

GPR is a common near-surface geophysical method with high resolution, high efficiency and non-destructiveness. It has been widely used to detect various fissures [19,20] in recent years. Eskandari et al. [21] analyzed the images of fissures detected by GPR using the SVD algorithm, and successfully reduced the clutter in the profile. They demonstrated that this method could detect fissures with a width greater than 1.3 mm, which proves that the GPR system can effectively detect road fissures in practice. Previous studies have also combined GPR with other techniques to detect different types of fissures. For example, Dorn et al. [22] detected the solute transport in the aquifer fissure using GPR and tracer test data, and obtained information on the number, connectivity and geometric characteristics of the fissures that contribute to the migration. Solla et al. [23] detected and described road fissures and their sources using GPR and infrared thermal imaging technology. They showed that this combination can detect road fissures more comprehensively and non-destructively.

Numerous logging techniques, including natural gamma logging, acoustic logging, and resistivity logging, have been extensively employed in the detection of fissures within rock masses [24–26]. Leal et al. [27] showed that the fractal dimension of resistivity image logging can effectively identify the fissures in the oil well formation of natural fractured reservoirs. They also applied the SVM model to automatically detect natural open fissures in resistivity image logging before the long interpretation process. Lopes et al. [28] used logging technology and three-dimensional GPR to characterize karst dissolution zone, fault network and formation interface in three dimensions. Tokhmechi et al. [29] introduced a novel approach to detect fracture zones and fissure density using water saturation log data. This approach employs wavelet transform and shale volume (or gamma) logging data to filter errors and estimate the number of fissures within each fracture zone. This method has been effectively implemented in four wells within an Iranian oil field, yielding positive results.

In addition to conventional logging methods, the borehole televiewer is a special logging technique that effectively detects rock mass fissures. Lau et al. [30] used subsurface fissure surveys with a borehole camera and acoustic televiewer to detect underground fissures. They demonstrated that borehole camera survey and acoustic televiewer logging is a fast, cost-effective and accurate method to measure fissures and their characteristics in boreholes ranging from 7.6 to 15.3 cm in diameter. Li et al. [31] employed a borehole televiewer to observe fissures within rock mass and detail the apparatus and operating procedures for this approach. Supported by case study data, the study concludes that borehole televiewer is an effective tool for observing fissures and that the proposed method yields accurate and dependable results.

GPR is commonly used for detecting fissures in cultural relics, while logging is rarely utilized in this context. Capineri et al. [32] used RASCAN holographic radar to detect subsurface defects, including fissures, in the decorative marble medallions of the Temple of San Biagio and frescoes in the Church of San Rocco in Italy. Hœrlé et al. [33] conducted a GPR survey of two rock art sites in the KwaZulu-Natal Drakensberg, South Africa, to assess the presence of cracks in the rock walls that could lead to destabilization. The findings demonstrate the radar's capability to locate potential crack formation areas. Masini et al. [34] employed ground-penetrating radar with a high-frequency antenna to analyze the internal structure of the rose window of Troia Cathedral. The results indicate that the GPR survey yielded valuable insights into the internal structure, including the detection of fissures and boundaries of previously repaired sections.

Although GPR and logging technology are commonly utilized for fissure detection, they possess certain limitations when used independently for detecting rock mass fissures. GPR is mainly applied to detect shallow targets in cultural relics [35]. When the detection target depth reaches more than ten meters, the GPR detection requires antenna frequencies below 200 MHz. At this frequency, the radar resolution is low, and there are numerous interference signals in the radar profile. The detection environment is complex and diverse, and GPR has technical limitations. These factors result in multiplicity and uncertainties in GPR interpretation, which prevent accurate detection of fissures in cultural relics. Conventional logging technology can only obtain information from the local area around the borehole,

with limited ability to obtain formation information from far away. The utilization of a borehole televiewer exclusively offers imaging data restricted to the surface of the borehole wall. Moreover, it is influenced by factors like fissures generated during drilling and wall debris, which impede its accuracy in detecting fissures and geological layers.

To investigate a refined detection method of fractures in the cave rock mass and improve the accuracy of fracture detection, this study introduces a ground-penetrating radar detection method with the logging data constraint. The method was applied to the detection of fracture diseases in the rock mass of Dazu Rock Carvings. Conventional logging and borehole televiewer data provided accurate information on geological stratification. By matching the GPR profile with the stratigraphic information, we obtained electromagnetic waves velocity of the strata. This improved the accuracy of depth interpretation in GPR profiles. The stratigraphic and fissure information obtained from logging data was utilized to verify the interpretation results of GPR. In addition, the verified anomalies in the GPR profile were used to infer other anomalies of the same type.

2. Materials and Methods

2.1. Study Area

The Dazu Rock Carvings are situated in the Dazu District of Chongqing, China, making them one of the eight largest grottoes in the world and the largest center of grotto art in China. In 1999, they were added to the list of world cultural heritage sites due to their significant historical, artistic, and scientific value. The carvings depict the development and evolution of grotto art in China during the Tang and Song Dynasties, spanning from the 9th to the 13th century. There are 23 sites scattered throughout the southwest, northwest, and northeast regions of the county, with the Baodingshan cliff statues being the most exquisite and largest among all the carvings. The Dafowan rock carvings area is a crucial part of these statues and serves as their primary concentration area. The study area is situated at the southern cliff top of Dafowan Bay in the Baodingshan Rock Carvings scenic spot of the Dazu Rock Carvings (Figure 1).

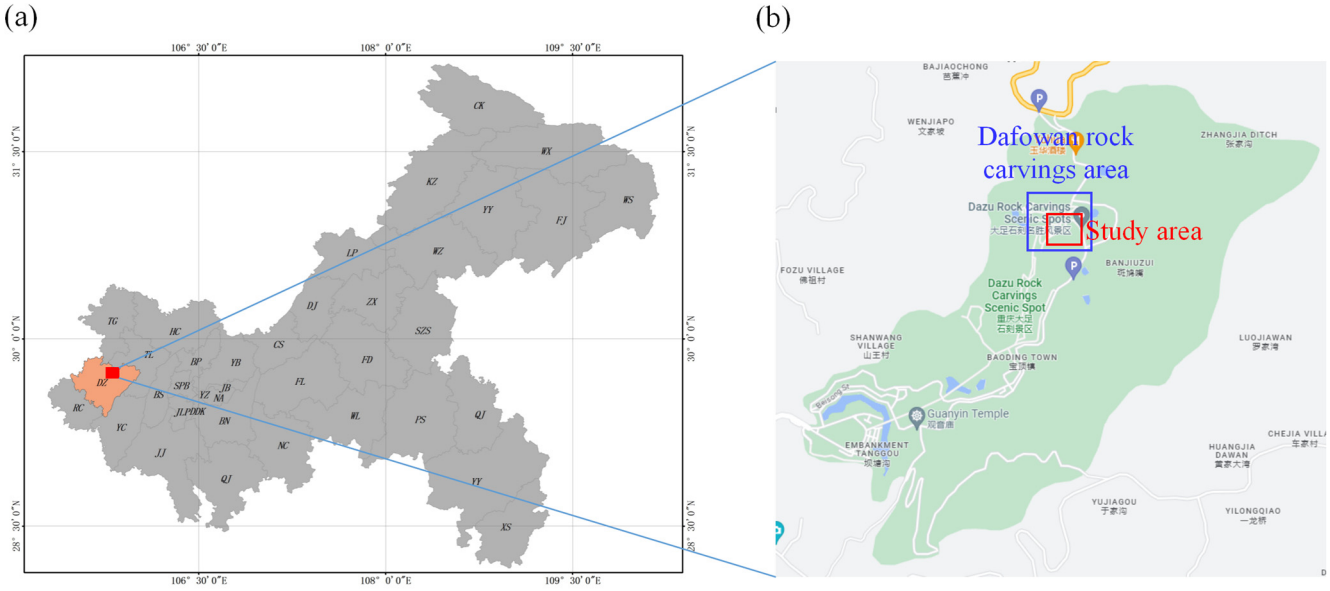

Figure 1. Location of the study area. (**a**) the location of Baodingshan Rock Carvings Scenic Spot in Chongqing; (**b**) the location of the study area in the Baodingshan Rock Carvings Scenic Spot (the blue line frame area is the Dafowan rock carvings area, and the red line frame area is the study area).

Figure 2a shows the geological profile of the study area based on geological data. The exposed strata in the study area are mainly sandstone, with a weak layer of shaly sand intercalated in the sandstone strata. The weak interlayer is a signature stratum that runs through the entirety of the Dafowan Bay. The overburden layer in the study area generally

has a double layer structure. The upper layer consists of loose artificial fill, and the lower layer consists of colluvial and residual deposits. The overburden layer on the south bank of Dafowan Bay is about 2–3 m thick. The structure of this area is relatively gentle, with nearly horizontal rock layers. The strata have good continuity, with dip angles mostly between 2° and 9°. After investigating this area, it was found that the fissures in this area are mainly tensile cracks, with no obvious shear crack observed. During the investigation, no faults or other large geological structures were found.

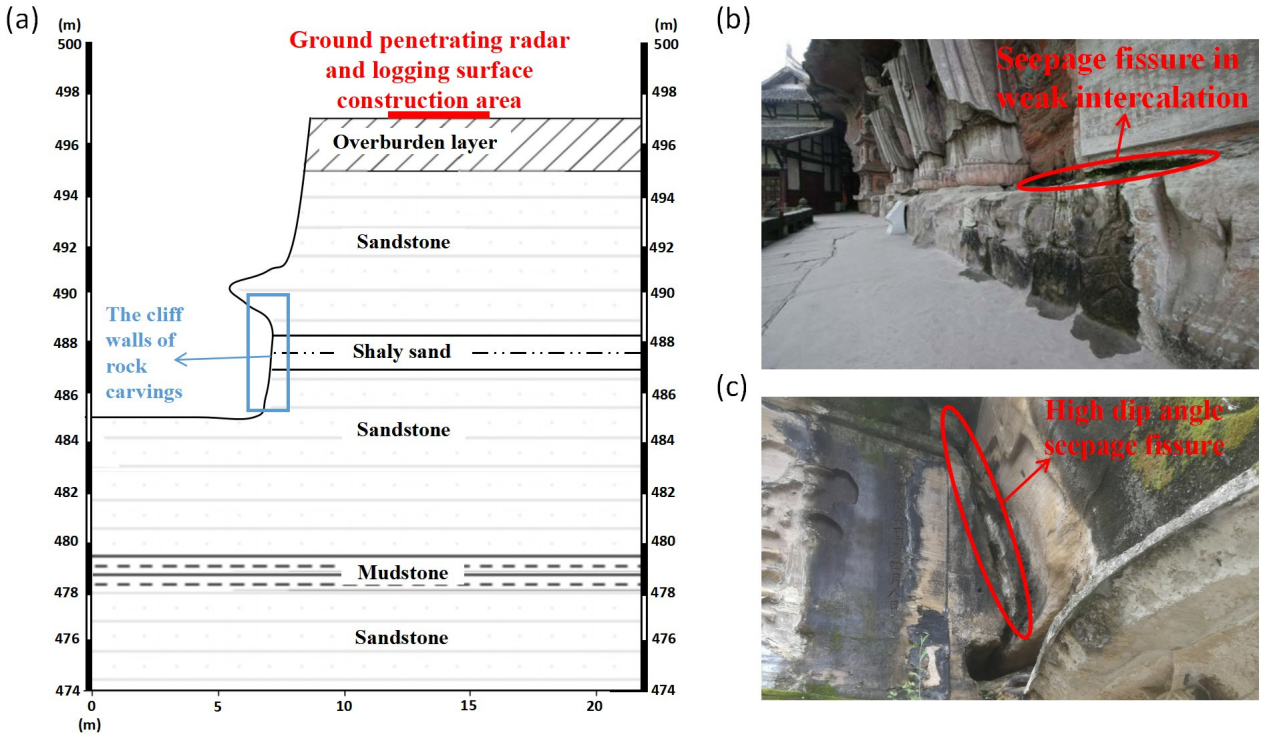

Figure 2. Geological profile map of the Dafowan rock carvings area and photos of fissures exposed on the cliff face. (**a**) Geological profile; (**b**) a seepage fissure exposed in the shaly sand layer of the cliff face; (**c**) a high dip angle seepage fissure exposed on the cliff face of rock carvings.

In recent years, the Dazu Rock Carvings have been severely affected by various diseases, among which the most obvious damage to the grottoes is caused by fissures and seepage. Figure 2b,c shows the fissures and seepage conditions exposed on the cliff face of the grotto statues. These fissures not only affect the aesthetics of the grottoes, but also seriously endanger the stability of the grotto rock mass. Despite repeated treatments, these seepage phenomena have not been completely and effectively solved so far. Under water pressure, water from different sources communicates with each other through unloading fissures, bedding fissures and weathering fissures encountered. These fissures form a seepage network, which makes the water spread throughout the grottoes. Therefore, an urgent problem for the current protection of the Dazu Rock Carvings cultural relics is how to detect the seepage fissures in the grotto rock mass effectively and non-destructively.

2.2. Data Acquisition

Six GPR survey lines (L1 to L6) were laid along the south cliff top road at Dafowan Bay and five drill holes (ZK1 to ZK5) were found near the survey lines. ZK3 was excluded from this survey due to its small diameter. Conventional logging and borehole televiewer surveys were conducted for the remaining four boreholes. RTK was used to accurately locate the endpoints of each survey line and the position of the borehole wellhead. This helped record their relative positions and facilitate comprehensive comparative analysis of later exploration data. Figure 3a shows the location of the GPR survey lines and boreholes.

Figure 3. (**a**) GPR survey lines and borehole locations in the study area; (**b**) GPR L6 survey line data acquisition using a MALA 100 MHz antenna; (**c**) borehole televiewer image acquisition in borehole ZK2 using a JKX-4A borehole full-wall imaging system.

Most fissures exposed on the cliff surface have a depth of 10–15 m. Initially, a 100 MHz GPR antenna was considered to achieve the required detection depth. With a formation electromagnetic wave velocity of 0.11 m/ns, an electromagnetic wave with a frequency of 100 MHz has a wavelength of 1.1 m. The resolution of GPR can be determined using the Huygens-Fresnel principle, which calculates it as one-fourth of the GPR wave's wavelength, resulting in a resolution of 0.275 m. This resolution meets the detection requirements for fracture zones. Ultimately, the Swedish MALA ProEx control unit and a 100 MHz GPR antenna were selected for detection based on their GPR detection depth and resolution. GPR data were collected using a single point measurement method with a distance interval of 0.1 m, a sampling time window of 500 ns, and a sampling frequency of 994.95 MHz. Figure 3b shows the on-site situation during GPR data collection.

Four conventional logging data were measured: natural gamma logging, well temperature logging, acoustic logging, and three lateral resistivity logging. The natural gamma value reflects the shale content in the stratum, which is useful for detecting the main seepage layer (weak interlayer of shaly sand). It can also be used to determine the location of water bearing strata [36]. Well temperature logging can help estimate the water level depth in the well. The acoustic logging curve is capable of reflecting the lithological and structural features of the formation. The resistivity logging curve reflects the rock type, permeability, and water content of the formation. Natural gamma ray, acoustic wave and resistivity logging are suitable for seepage fissure detection and fracture zone exploration due to their distinct characteristics and advantages. We used JGS-6 integrated digital logging system and JKX-4 A borehole wall imaging system produced by CGE(Chongqing)Geological Instrument Co., Ltd. to acquire conventional logging data and borehole televiewer images. Figure 3c shows the borehole televiewer image scene photo.

2.3. Single Geophysical Method Data Analysis

2.3.1. Ground-Penetrating Radar

The collected GPR data were processed using Reflexw software for DC removal, zero correction, gain and bandpass filtering. This produced a GPR profile that allowed for easy determination of formation interfaces. Figure 4 illustrates the GPR profiles before and after processing the data from the L2 and L3 survey lines. Formation interfaces can be determined based on characteristic changes of reflected signals [37] as the reflection characteristics of

electromagnetic waves vary among strata of different lithologies. The lithology of the strata can then be determined in conjunction with the available geological information. According to geological data and logging information, the shale content in the deep part of the shaly sand layer is relatively low, which exhibits high similarity to the geophysical properties of the sandstone layer. In addition, severe energy attenuation of radar waves through the shaly sand layer, so no clear reflection signal is observed at the interface between the shaly sand and the lower sandstone layer in the profile. Therefore, we did not mark this interface during stratigraphic interpretation. The remaining survey lines exhibit geological stratification characteristics similar to those of the L2 and L3 survey lines.

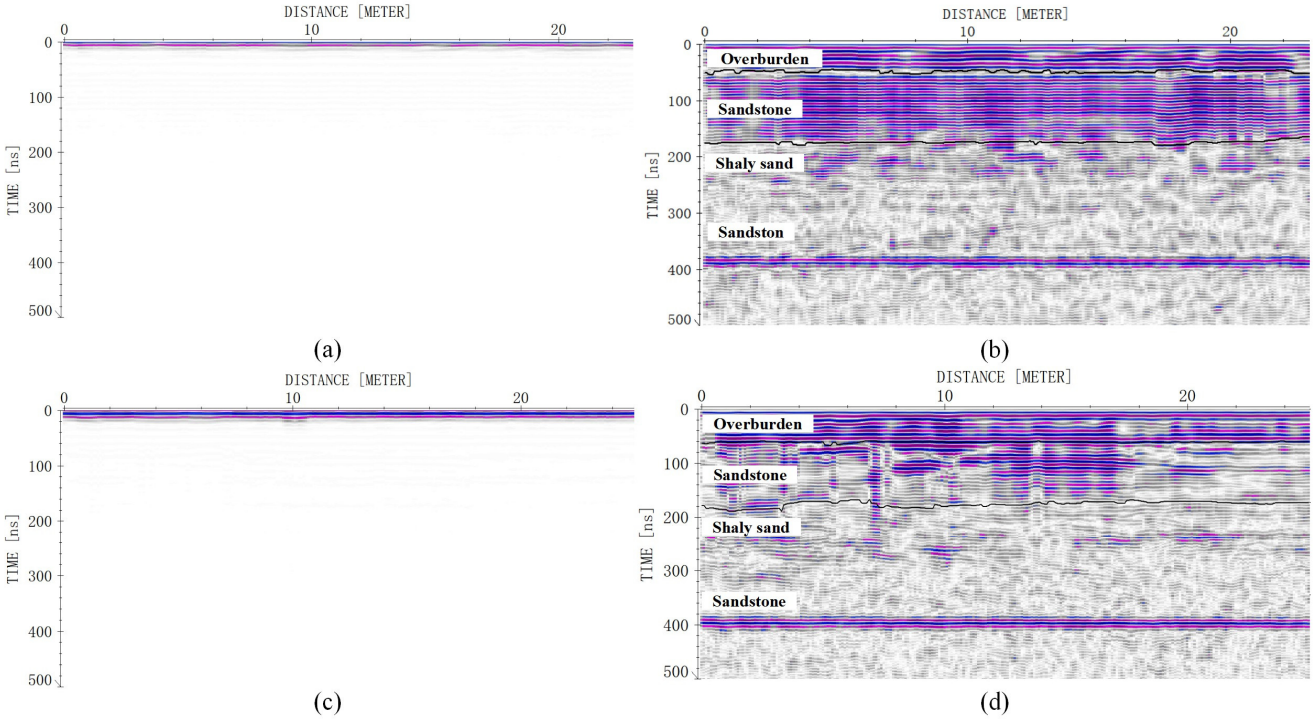

Figure 4. GPR profiles before and after data processing. (**a**) Original GPR profile of the L2 survey line; (**b**) GPR profiles of the L2 survey line showing lithological stratification; (**c**) original GPR profile of the L3 survey line; (**d**) GPR profiles of the L3 survey line showing lithological stratification.

We chose the GPR profile of the L2 survey line shown in Figure 4b for our analysis. An obvious change in the characteristics of reflection events is observed at a depth of 45 ns within the L2 survey line profile. By combining geological data, this area has been identified as the interface between overburden and sandstone. At a depth near 180 ns within the profile, an abrupt change in both reflected wave energy and event continuity is observed. By combining the geological profile of the survey area, this region has been identified as the interface between sandstone formation and shaly sand formation. A strong and perfectly horizontal reflection event is observed at 390 ns within the profile and is consistently present at this location across all six survey lines. Given this consistency, it has been identified as an interference signal originating from detection equipment.

Profiles from survey lines L1 to L6 were synthesized into a single profile, to which the same data processing steps were applied. Subsequently, lithological interpretation of the profile was conducted. Figure 5 presents the resulting combined profile, inclusive of annotated stratigraphic boundaries. As shown in Figure 5, good continuity is observed between the different line profiles for the two stratigraphic interfaces mentioned above. Stratification results from the combined profile indicate good continuity among strata within the study area and an absence of large structural faults, which is consistent with the stratigraphic description present within geological data.

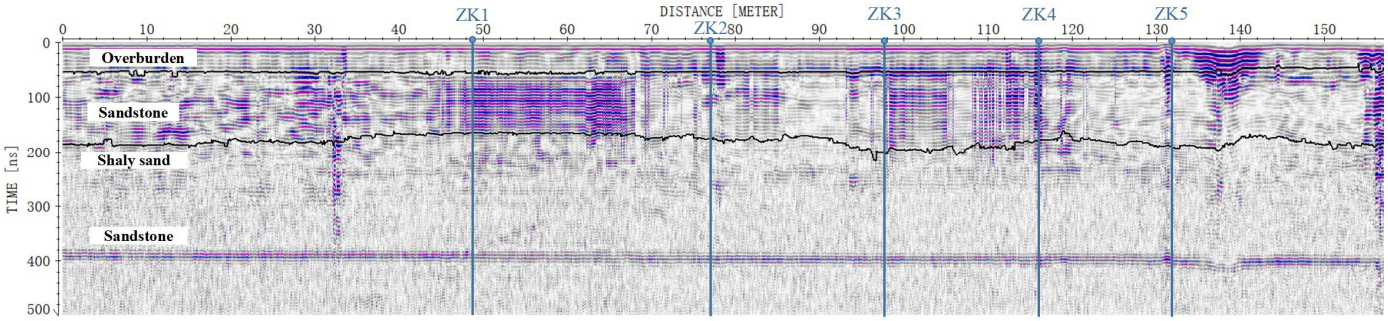

Figure 5. The profile of the L1 to L6 survey line after splicing and its lithological stratification.

A GPR profile, obtained through the performance of background removal in addition to the aforementioned data processing steps, is better suited for the identification of anomalies. Figure 6 illustrates the GPR profiles of the L2 survey line before and after removing the background.

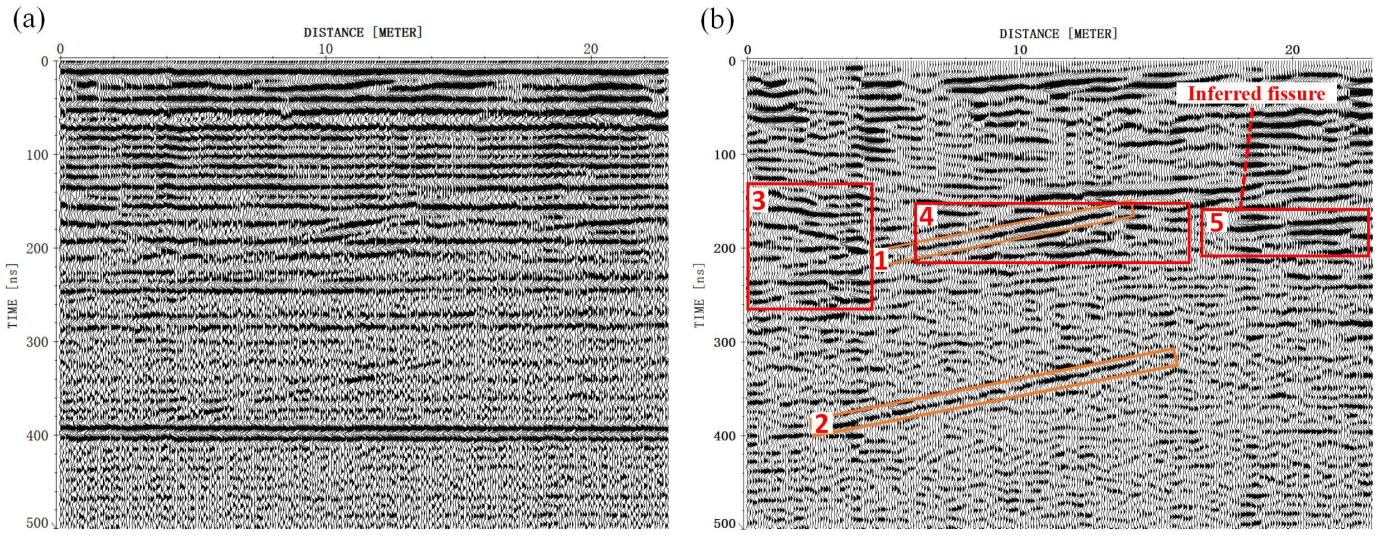

Figure 6. (**a**) GPR profile of the L2 survey line before background removal; (**b**) the L2 survey line profile after background removal and its geological interpretation.

Survey line L2 was also selected for analysis, as depicted in Figure 6b. A strong amplitude signal, extending from the ground to a depth of 400 ns, is present at a distance of 3.9 m from the starting point within the L2 profile. Owing to its proximity to ZK1 borehole, this strong amplitude signal has been identified as interference originating from the borehole. Straight linear events are depicted within regions No.1 and No.2 of the figure. Given the complexity of underground media and structures, we believe that these events represent not reflected waves from underground structures but rather interference signals reflected from surface objects. Reflection events within regions No.3 to No.5 exhibit characteristics including dislocation, strong amplitude, low frequency, and oscillation; it is thus inferred that rock mass within these areas may represent water-bearing fracture zones or strata with high shale content. Within the range of 50–150 nanoseconds along the L2 survey line, a significantly stronger reflection signal was observed in the 18–19 m area. Meanwhile, we found a high-dip seepage fissure on the corresponding cliff face, as shown in Figure 2c. Therefore, we surmised that near-vertical seepage fissure may exist here. Reflection events in other areas of the profile are weak in comparison, indicating good rock integrity in these areas.

2.3.2. Conventional Logging

Prior to lithology interpretation of logging data, preprocessing is required including depth alignment, correction of inclined well curves to vertical well curves, curve smoothing, environmental correction, and numerical standardization [38]. Sandstone and mudstone can be distinguished by characteristics of acoustic interval transit time curves, natural gamma curves, and resistivity curves in conventional logging [39].

Following interpretation of the lithology of the logging data using the characteristics of three types of logging curves, a ZK4 borehole logging lithology interpretation diagram was generated, as shown in Figure 7. The diagram indicates that shallow strata above 11 m near the ZK4 borehole primarily consist of sandstone with low shale content. At depths of 11–20 m, shaly sand and sandstone formations are interbedded within formations. Below a depth of 20 m, a thick layer of mudstone is present.

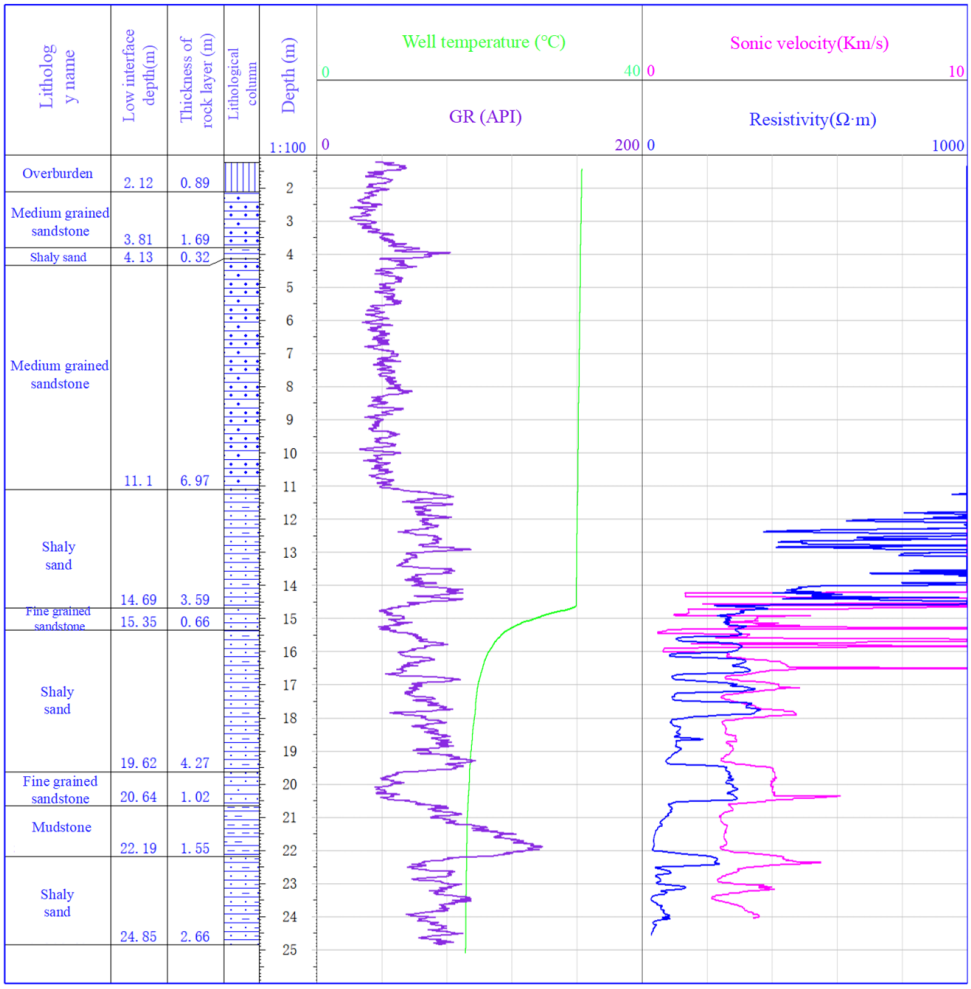

Figure 7. ZK4 borehole logging lithology interpretation diagram.

Observations on the cliff indicate that the shaly sand formation is the primary water seepage layer, with clear indications on the logging curve. As a result, we use the interface between this stratum and the overlying sandstone formation as a marker for cross-well stratigraphic correlation. Based on wellhead elevation data measured by RTK, we determined each borehole's relative height and created a stratigraphic correlation diagram for four boreholes, as shown in Figure 8. The figure shows that the area has good stratigraphic continuity. Additionally, shaly sand formation thickness varies among boreholes. From south to north, formation lithology uniformity decreases, and shale becomes more widely distributed within the formation.

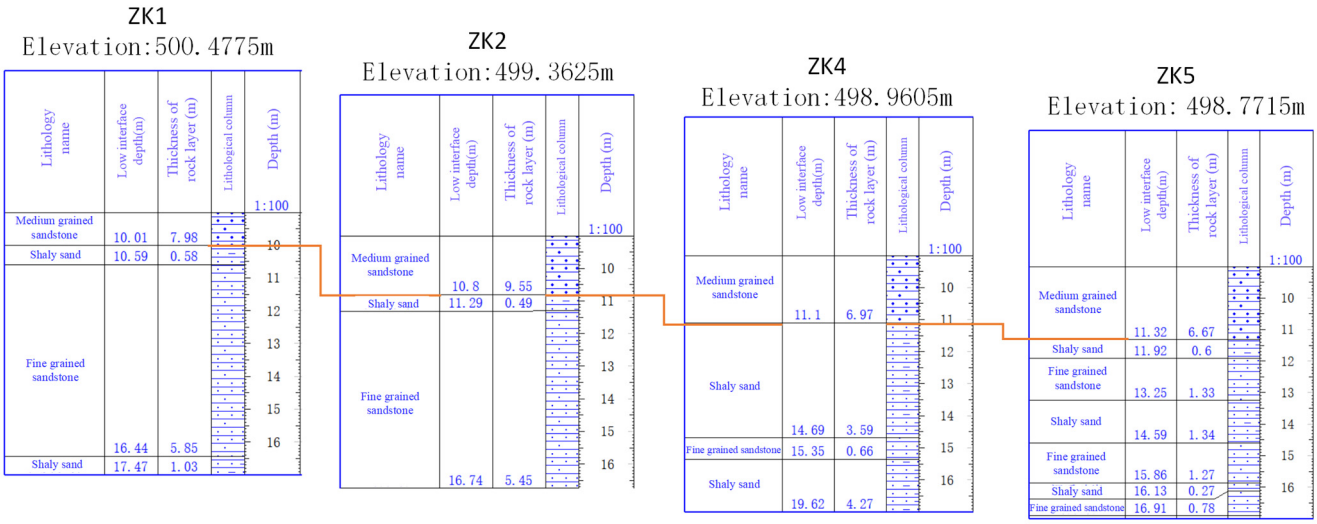

Figure 8. The stratigraphic correlation of ZK1, ZK2, ZK4 and ZK5 boreholes.

2.3.3. Borehole Televiewer

To obtain borehole wall images for analysis, borehole televiewer data requires only depth correction. High-definition borehole images obtained using borehole televiewer technology can help us observe changes in formation lithology and understand the distribution of fissures and fracture zones [40]. For single fissure surfaces observed in borehole televiewer images, we use borehole wall imaging system analysis software to fit the fissure edge curve. Through a series of calculations of the fitted curve by this software, we can obtain information about the depth range, dip angle and azimuth angle of the fissure surface. In addition, this software allows for manual extraction of fissure width data. Figure 9 displays a section of a ZK2 borehole televiewer image and its associated fissure surface occurrence information.

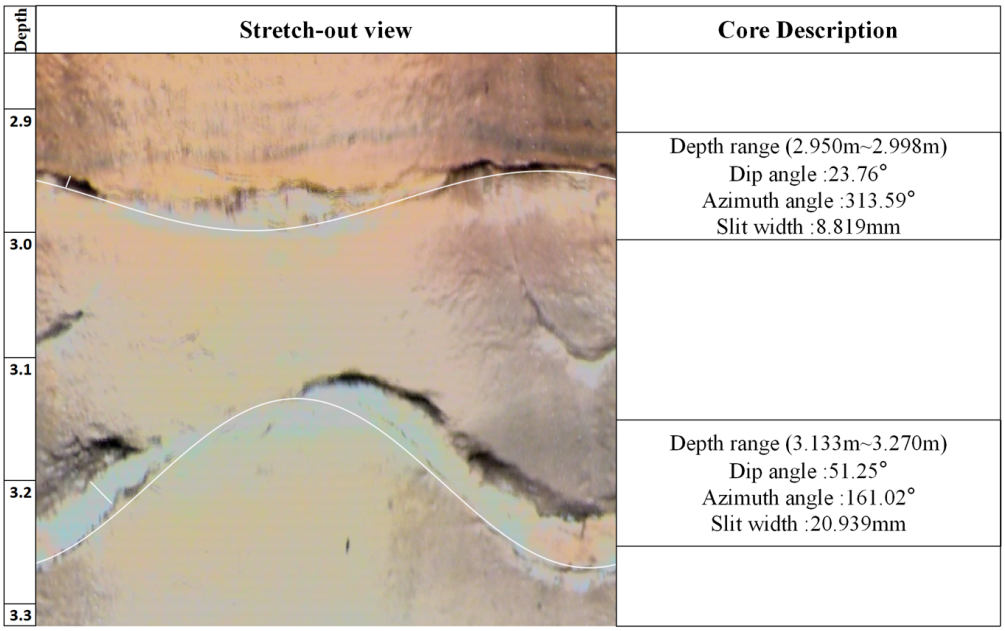

Figure 9. ZK2 borehole televiewer image and fissure plane occurrence information within 2.9~3.3 m depth of ZK2 borehole.

Rock mass fissure occurrence data were obtained from the borehole walls of four boreholes using the software. The data underwent classification, organization, and statistical analysis to produce the fissure occurrence statistics graph depicted in Figure 10. Preliminary analysis of the graph data revealed several characteristics of fissure occurrence parameters within the measurement zone. Fissures were primarily distributed within an intermediate depth range of 8–16 m. Low dip angle fissures predominated, and no apparent patterns were observed in the dip direction distribution of fissure surfaces.

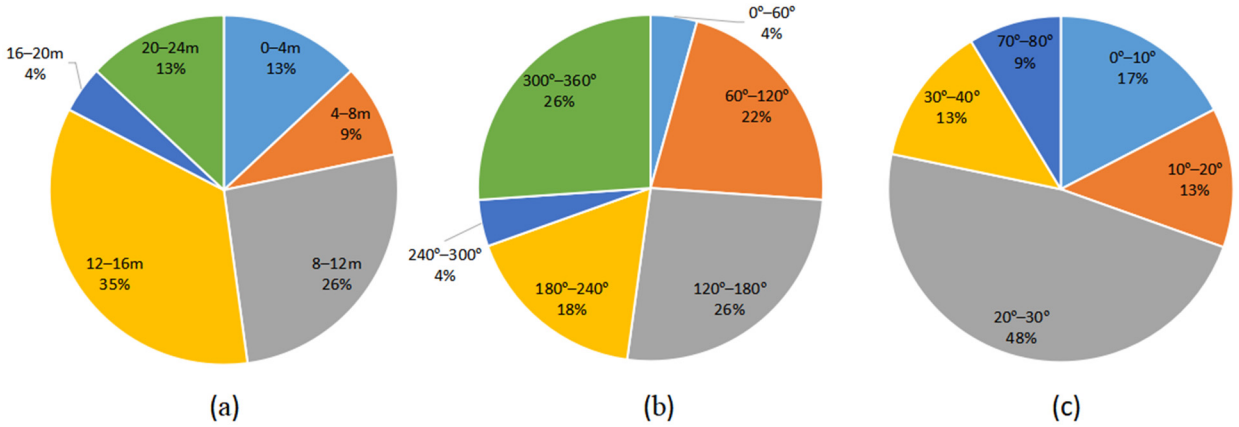

Figure 10. Pie chart of wellbore fissure occurrence parameters. (**a**) Pie chart of fissure depth distribution; (**b**) pie chart of dip direction distribution of fissure surfaces; (**c**) pie chart of dip angle distribution of fissure surfaces.

3. Results

3.1. Comprehensive Analysis of Borehole Data

Before using borehole data to compare and verify the content of GPR data interpretation, we should comprehensively analyze logging data to improve the reliability of borehole data. Geological environments are often more complex in reality. Similar logging curve characteristics may correspond to different stratigraphic structures and combinations. Although borehole televiewer images are intuitive, they may contain false targets and can be challenging to distinguish. For example, the borehole wall may be contaminated by mud, the imaging of the borehole wall after weathering is different from that of the original borehole wall, and the fracture of the borehole wall during drilling. Therefore, a comparative analysis of conventional logging and borehole televiewer data is necessary for the interpretation of strata and fissures using borehole data.

To eliminate interfering information, data from both conventional logging and borehole televiewer were compared at the same depth. The final composite logging interpretation of borehole ZK4 is illustrated in Figure 11. The depth of the stratigraphic interface and the lithology of the strata in the conventional logging interpretation diagram are in general agreement with those on the borehole televiewer images.

Fracture zones can be clearly characterized by physical parameter from various logging curves. The development of fissures in formations and rocks can cause volume loosening, increased porosity, and enhanced permeability, resulting in changes in physical parameters. In conventional logging curves, the fracture zone primarily manifests as a comb-like high and low value anomalous response in sonic time difference curves and multiple low value anomalous responses in apparent resistivity curve anomalies. Figure 11b shows the interpretation of borehole ZK4′s logging lithology. The interval from 15.3 to 16.3 m coincides with logging characteristics of a fracture zone and is thus interpreted as such. The borehole televiewer image in Figure 11a at the corresponding depth confirms this interpretation.

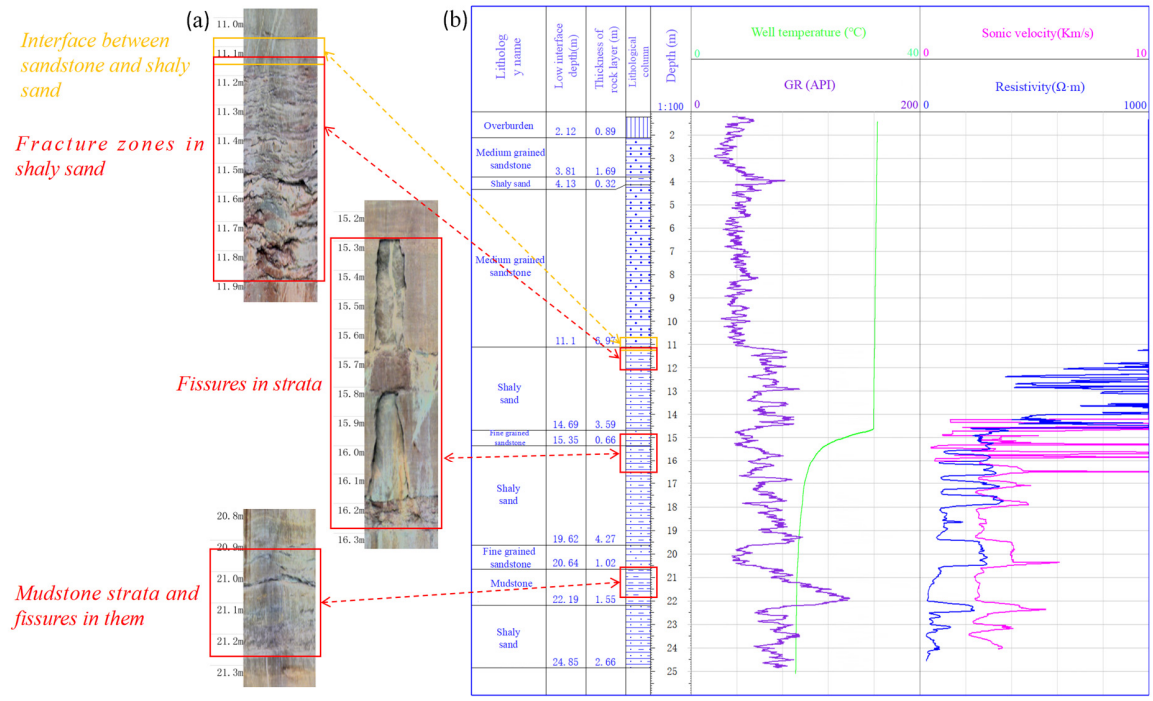

Figure 11. Comparative analysis chart of information of borehole. (**a**) Borehole televiewer image of ZK4 borehole; (**b**) logging lithological interpretation of ZK4 borehole.

3.2. Obtain Formation Electromagnetic Wave Velocity

During previous exploration work within the research area, formation electromagnetic wave velocity was calibrated by scholars based on overburden layer thickness obtained during drilling and corresponding radar reflection time. The calibration results indicated that an electromagnetic wave velocity of 0.07 m/ns is more suitable for the overburden of the study area. Regrettably, the electromagnetic wave velocity values of the strata beneath the overburden have not undergone calibration.

Since the L4 GPR line is near ZK4 borehole, we matched the L4 line's lithological interpretation profile with the ZK4 borehole televiewer image (Figure 12). We previously determined interface depth between sandstone and shaly sand formation accurately using borehole televiewer images and conventional logging curves. Strata electromagnetic wave velocity was calibrated using this depth value and the corresponding radar reflection time. This allowed for the calculation of GPR wave velocity for sandstone layers and average electromagnetic wave velocity for strata above interfaces near boreholes, respectively.

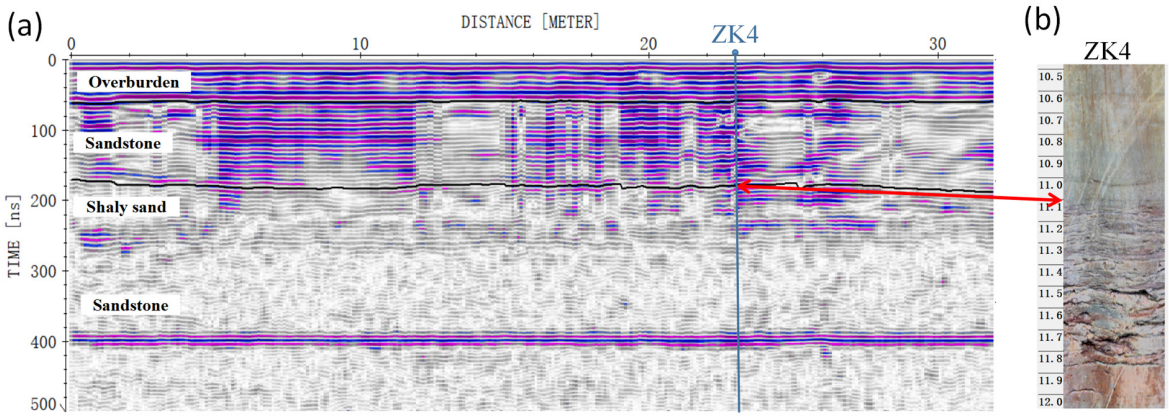

Figure 12. Comparison of GPR profile lithological interpretation and borehole televiewer image. (**a**) GPR L4 line profile and its lithological interpretation; (**b**) partial image of borehole televiewer for ZK4 borehole.

For the L2 and L3 lines in proximity to the borehole, strata matching, and electromagnetic wave velocity calculations were performed as previously described, with the obtained velocities recorded in Table 1. The average wave velocities presented in Table 1 indicate that the electromagnetic wave velocity of the sandstone formation is approximately 0.135 m/ns, while the average electromagnetic wave velocity for strata above the shaly sand formation is approximately 0.116 m/ns. These data can aid in more accurately determining the depth of anomalies during time-depth conversion of GPR profiles.

Table 1. Statistical table of electromagnetic wave velocity of the strata in the study area.

Survey Line Number	Sandstone Formation Velocity	Average Velocity
L2	0.135 m/ns	0.117 m/ns
L3	0.134 m/ns	0.114 m/ns
L4	0.136 m/ns	0.118 m/ns
average value	0.135 m/ns	0.116 m/ns

3.3. Integrated Interpretation

The interpretation of GPR data has multiplicity and can be affected by interference signals that may obscure anomalies or create false ones. Borehole televiewer images can accurately identify fissures in the borehole wall and provide their location information, thereby effectively verifying and supplementing the interpretation of GPR anomalies. In Section 3.1 of this paper, borehole televiewer images of fissures were verified by conventional logging to ensure accurate identification of fissures.

In our previous analysis of processed radar profiles, we examined and eliminated certain interference signals and conducted a preliminary interpretation. However, there was a high degree of uncertainty in the interpretation. To verify the previous interpretation results and accurately locate anomalous areas, we compared the preliminary interpretations of the profiles with borehole televiewer images. In certain areas of the same radar profile, events were found to be connected to those at the borehole location and exhibited similar characteristics. These areas could be interpreted as exhibiting the same anomaly as their corresponding borehole locations due to the continuity of shaly sand formations and fissures within a limited range of rock mass. Furthermore, geological characteristics within the same formation generally remain consistent over distances spanning tens of meters. Consequently, verified anomalies can be utilized to interpret areas that are distant from the borehole location but exhibit similar anomaly characteristics within the same profile.

We used the average GPR wave velocity of the strata calculated in Section 3.2 to estimate the depth values in the GPR profiles preliminarily. Figure 13 compares the borehole televiewer anomaly images of ZK1 with the GPR interpreted profile of Line L2. In Figure 13a, the borehole televiewer image information at depths between 10.3–10.8 m, 13.8–15.3 m, and 18.7–19.5 m in borehole ZK1 corresponds to regions No.1, No.2, and No.3 in Figure 13b, respectively. Based on this analysis, we determined that region No.1 corresponds to a weak interlayer of shaly sand containing fissures, region No.2 represents shaly sand with a few horizontal fissures, and region No.3 is constituted of shaly sand with a fracture zone. There are also strong reflection signals with similar characteristics in the area far from the borehole. For example, the regions No.4 and No.5 in the figure are similar to region No.1. Therefore, regions No.4 and No.5 are also interpreted as weak interlayers of shaly sand and containing fissures.

Using the interpretation principle and analysis method of line L2, we conducted a comprehensive interpretation of the remaining lines. Figure 14 shows the results of comparing the borehole televiewer anomaly images of ZK4 borehole with the interpretation of the L4 GPR profile. The two anomalies below a depth of 15 m have unclear signals in the GPR profile. These anomalies were identified through Borehole televiewer images.

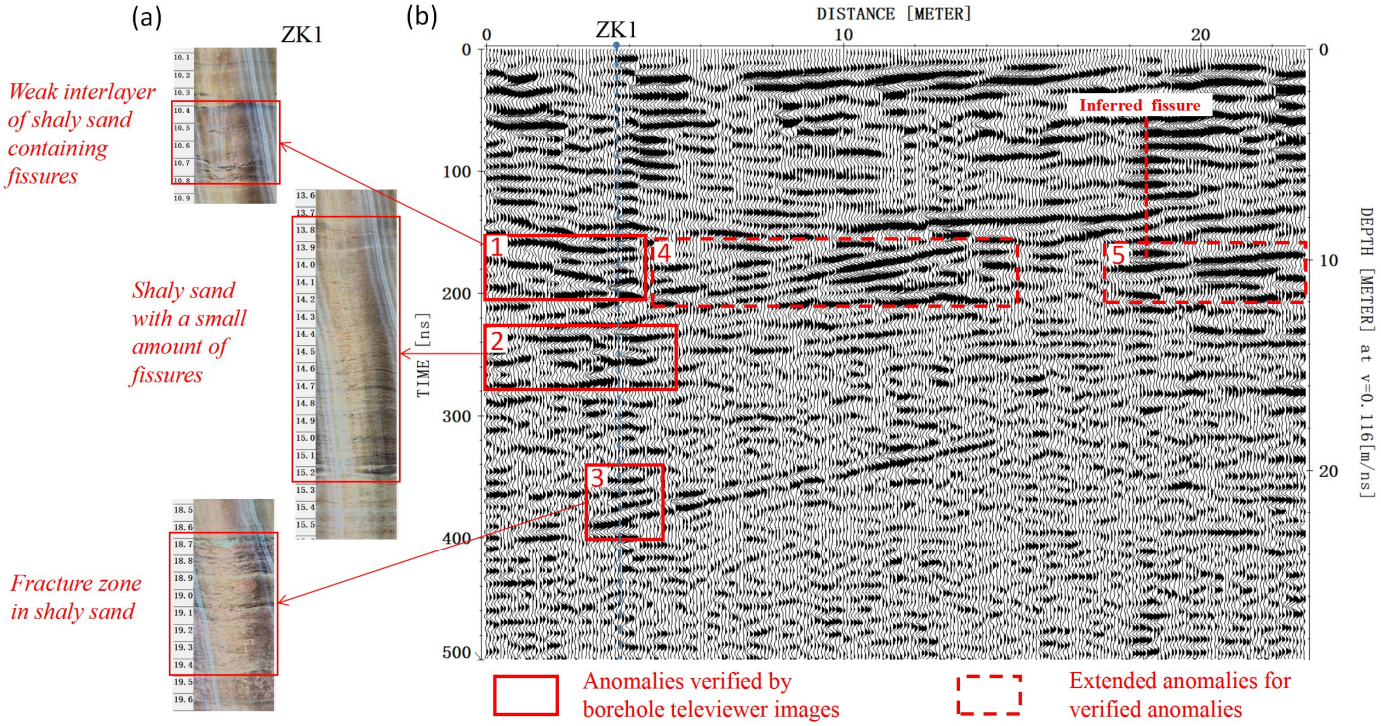

Figure 13. Comparison of borehole televiewer images from ZK1 borehole with L2 GPR profile interpretation. (**a**) ZK1 borehole televiewer fissure images; (**b**) L2 GPR survey line profile and its geological interpretation.

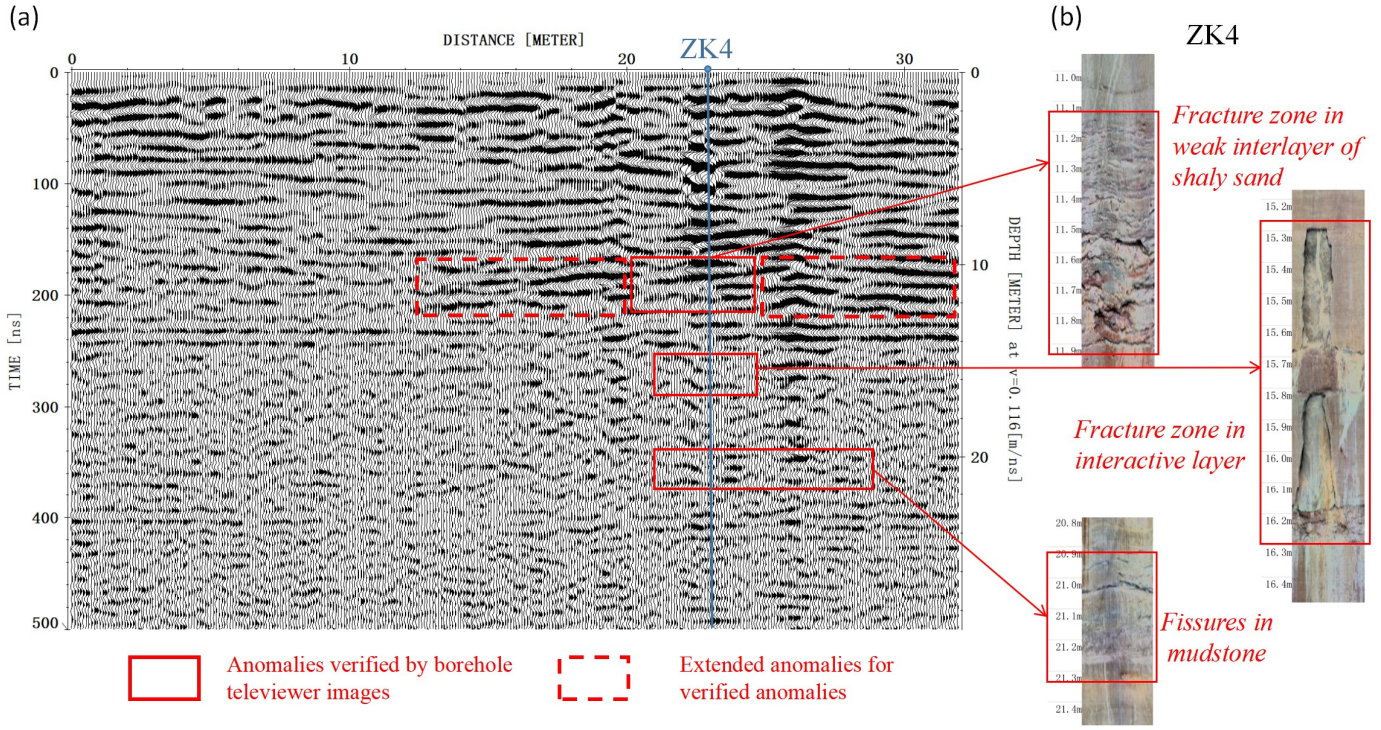

Figure 14. Comparison of borehole televiewer images from ZK4 borehole with L4 GPR profile interpretation. (**a**) L4 GPR survey line profile and its geological interpretation; (**b**) ZK4 borehole televiewer fissure images.

In order to conduct a comprehensive analysis of the geological conditions present within the study area, stratigraphic information, fracture zones, and structural fissures obtained from previous sections were plotted on a profile. The depth values of the profile were calculated utilizing electromagnetic wave formation velocities from both overburden and sandstone layers. This methodology provides a higher degree of accuracy for interpreting anomaly depth when compared to conventional methods that rely on estimated average velocities of strata for depth calculation. Comprehensive geological interpretation profiles for lines L2 and L4 are presented in Figures 15 and 16, respectively.

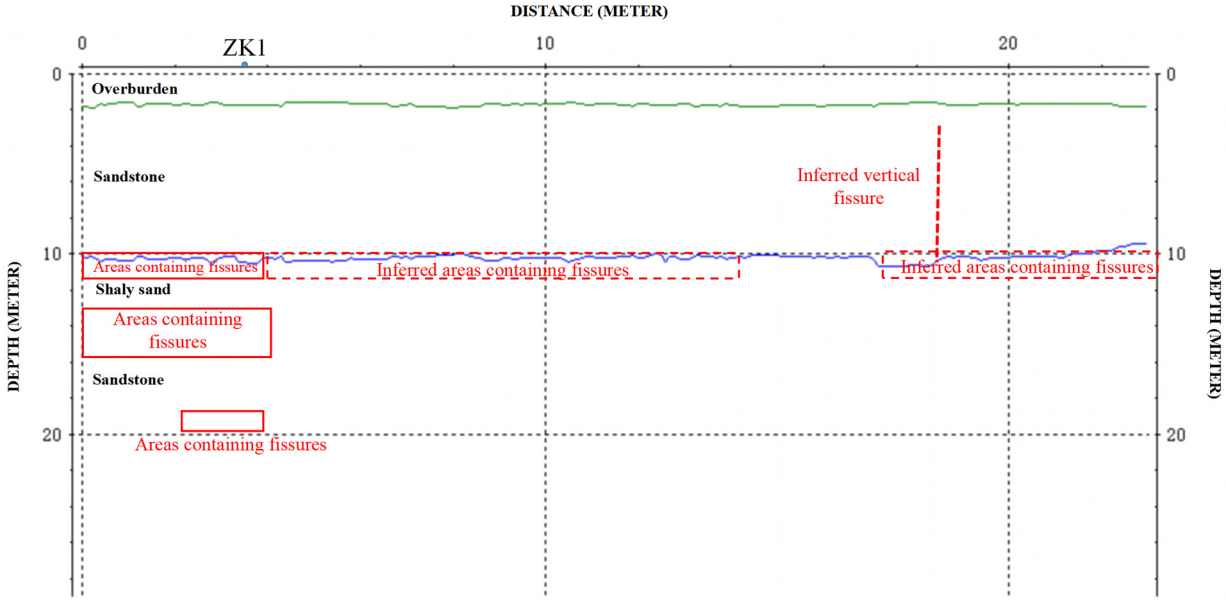

Figure 15. L2 survey line comprehensive geological interpretation profile.

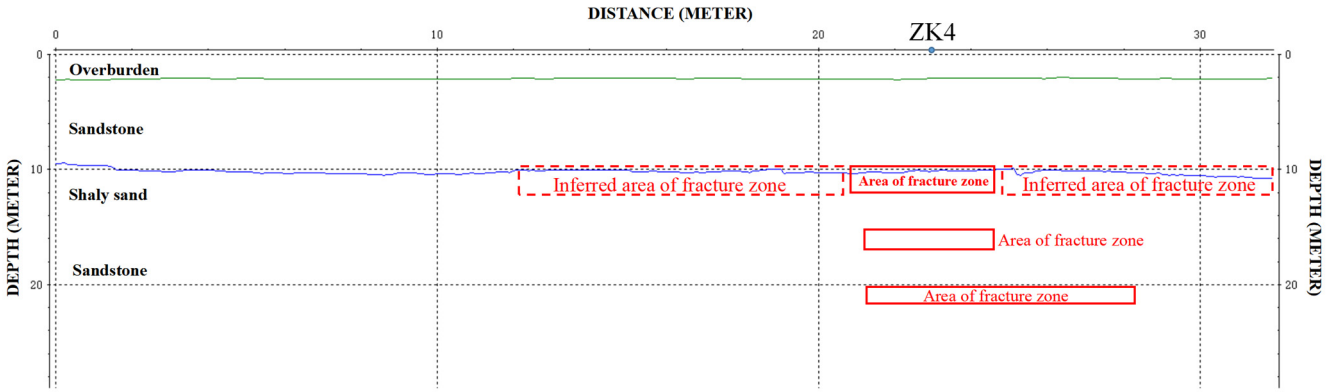

Figure 16. L4 survey line comprehensive geological interpretation profile.

Combining the seepage fissure information observed on the cliff face (Figure 2), borehole televiewer seepage fracture images, and the comprehensive geological interpretation profiles, we make the following speculations.

The shallow rock mass, ranging from 2 to 10 m in depth and located within the southern cliff area of Dafowan Bay, exhibits relatively good integrity. Within the shaly sand formation, at depths ranging from 10 to 12 m, well-developed fissures are present which may serve as horizontal seepage channels. Fissures are present within the rock mass at depths ranging from 15 to 22 m; however, these fissures exhibit poor continuity. Steeply dipping structural fissures are also present within the sandstone layer and may serve as channels for water infiltration from shallow to deeper sections.

4. Discussion

This paper focuses on the application of GPR detection method constrained by logging data for the detection of fractures in the cave rock mass. We present a novel methodology for the detection of fissures within rock relics, thereby enhancing technical capabilities within the field of relic disease detection and providing a valuable reference for related applications. According to our research findings, the proposed approach is effective in detecting water-bearing fissures and fracture zones within sandstone grottoes.

In previous GPR detections, empirical GPR wave velocity was commonly used for time-depth conversion. However, this method was often influenced by subjective factors during wave velocity selection, which led to inaccurate depth data. The detection method employed in this study successfully resolves this issue. Accurate depth data of stratigraphic boundaries was obtained by integrating data from conventional logging and borehole televiewer. By combining these data with GPR profiles, the GPR wave velocity for time-depth conversion was calculated, providing accurate depth data for the final GPR interpretation profiles.

Compared with the conventional GPR detection method, the proposed approach exhibits distinct advantages with respect to the credibility of anomaly interpretation. GPR techniques are highly effective for the detection of shallow geological targets, however, these techniques exhibit a degree of multiplicity when interpreting anomalies and are susceptible to external interference, potentially resulting in the generation of false anomalies. Conventional logging techniques can be utilized to accurately determine the location of stratigraphic interfaces, while borehole televiewer techniques can be employed to accurately identify fissures and obtain associated location information. However, the range of detection for logging methods is limited to a small area in close proximity to the borehole. With respect to the detection of grotto relics, the number of available boreholes is greatly limited, thereby further restricting the range of detection for logging methods when applied to relic detection. The joint application of GPR, conventional logging, and borehole televiewer techniques can effectively mitigate issues associated with GPR multiplicity and the limited range of detection for logging methods. Comprehensive data obtained from boreholes can serve to verify GPR interpretation content, while GPR profiles are capable of detecting areas that are not accessible via boreholes. This enables a more comprehensive and reliable approach for the detection of rock mass fissures and evaluation of rock integrity.

The detection method proposed in this paper also has certain limitations. Firstly, boreholes used to provide constraint information generate reflected signal on the GPR profile, which can cause certain interference to the GPR data. As the distance between boreholes and GPR survey lines decreases, the correlation between their data increases. However, this closer proximity also results in an increase in the strength of interference signals caused by boreholes within GPR data. In addition, the limited number of boreholes resulted in some areas where the results of the GPR interpretation could not be verified by the logging data. Therefore, the proposed approach in this paper still has certain uncertainties for the GPR interpretation of areas outside the range of logging data validation, and other subsequent detection methods are needed to verify the interpretation results. Finally, when low-frequency GPR antennas are utilized for the detection of fissures with large depth, the resolution of GPR is low, and the detection effect of narrow fissures is poor. In order to address these limitations, future research may consider the implementation of more effective noise-suppressed methodologies for the reduction in borehole interference on GPR data. Furthermore, the integration of more effective non-destructive detection technologies may facilitate the acquisition of more comprehensive and accurate detection results.

5. Conclusions

This study proposes a GPR detection method with the logging data constraint for the detection of fractured rock mass within the Baodingshan scenic area of the Dazu Rock Carvings, Chongqing, China. Initially, through the comparison of conventional logging data with borehole televiewer data, information pertaining to stratigraphic lithology and borehole wall fissures can be obtained. Subsequently, GPR profiles and borehole stratigraphic data were combined for the purpose of calibrating electromagnetic wave velocities of the strata in the study area. Utilizing calibrated stratigraphic electromagnetic wave velocities, accurate anomaly depth values can be calculated. Finally, a comparison of GPR profiles with borehole televiewer images can serve to verify and complement anomalies interpreted within GPR profiles. The results of the detection indicate that numerous fissures have developed in the shaly sand formation at a depth of 10–12 m in the southern cliff of Dafowan Bay. These fissures may be horizontal seepage channels. Additionally, some structural fissures exhibiting large dip angles are present within the sandstone layer and may serve as vertical seepage channels. The shaly sand formation exhibits poor rock mass integrity and fracture zones are evident within certain areas.

The GPR detection method with the logging data constraint used in this study allows for the validation and supplementation of GPR detection. This reduces the influence of the ambiguity and false anomaly of GPR on the detection results to a certain extent. This non-destructive detection method improves the accuracy of GPR rock mass fracture detection, providing new technical means and ideas for the protection and restoration of large stone cultural relics, such as grottoes.

Author Contributions: Conceptualization, W.Y., S.L., Q.Z., L.D. and Q.L.; methodology, W.Y. and S.L.; validation, S.L., L.D. and Q.L.; formal analysis, W.Y. and S.L.; investigation, W.Y., S.L., Q.Z. and L.P.; writing—original draft preparation, W.Y. and S.L.; writing—review and editing, S.L., L.D., Q.L. and Z.L.; visualization, W.Y., S.L. and L.P.; supervision, W.Y., L.D. and Q.L.; project administration, S.L. and L.D.; funding acquisition, S.L. All authors have read and agreed to the published version of the manuscript.

Funding: This research was funded by National Key Research and Development Program of China (grant number: 2021YFC1523401).

Data Availability Statement: Not applicable.

Acknowledgments: The authors would like to thank the editors and reviewers for providing their valuable comments and suggestions. In addition, the author would like to thank those involved in field data collection.

Conflicts of Interest: The authors declare no conflict of interest.

References

1. Liu, H.; Wang, X.; Guo, Q.; Zhang, M.; Wang, Y. Experimental Investigation on the Correlation between Rainfall Infiltration and the Deterioration of Wall Paintings at Mogao Grottoes, China. *Bull. Eng. Geol. Environ.* **2020**, *79*, 1199–1207. [CrossRef]
2. Lu, K.; Li, Z.; Niu, R.; Li, F.; Pan, J.; Li, K.; Chen, L. Using Surface Nuclear Magnetic Resonance and Spontaneous Potential to Investigate the Source of Water Seepage in the JinDeng Temple Grottoes, China. *J. Cult. Herit.* **2020**, *45*, 142–151. [CrossRef]
3. Rasol, M.A.; Pérez-Gracia, V.; Solla, M.; Pais, J.C.; Fernandes, F.M.; Santos, C. An Experimental and Numerical Approach to Combine Ground Penetrating Radar and Computational Modeling for the Identification of Early Cracking in Cement Concrete Pavements. *Ndt E Int.* **2020**, *115*, 102293. [CrossRef]
4. Grasmueck, M. 3-D Ground-penetrating Radar Applied to Fracture Imaging in Gneiss. *Geophysics* **1996**, *61*, 1050–1064. [CrossRef]
5. Tang, C.-S.; Wang, D.-Y.; Zhu, C.; Zhou, Q.-Y.; Xu, S.-K.; Shi, B. Characterizing Drying-Induced Clayey Soil Desiccation Cracking Process Using Electrical Resistivity Method. *Appl. Clay Sci.* **2018**, *152*, 101–112. [CrossRef]
6. Gélis, C.; Noble, M.; Cabrera, J.; Penz, S.; Chauris, H.; Cushing, E.M. Ability of High-Resolution Resistivity Tomography to Detect Fault and Fracture Zones: Application to the Tournemire Experimental Platform, France. *Pure Appl. Geophys.* **2016**, *173*, 573–589. [CrossRef]
7. Xu, Z.; Xin, H.; Weng, Y.; Li, G. Hydrogeological Study in Tongchuan City Using the Audio-Frequency Magnetotelluric Method. *Magnetochemistry* **2023**, *9*, 32. [CrossRef]

8. Sun, Y.; Zhai, C.; Xu, J.; Cong, Y.; Qin, L.; Zhao, C. Characterisation and Evolution of the Full Size Range of Pores and Fractures in Rocks under Freeze-Thaw Conditions Using Nuclear Magnetic Resonance and Three-Dimensional X-ray Microscopy. *Eng. Geol.* **2020**, *271*, 105616. [CrossRef]
9. Dijk, P.; Berkowitz, B.; Bendel, P. Investigation of Flow in Water-Saturated Rock Fractures Using Nuclear Magnetic Resonance Imaging (NMRI). *Water Resour. Res.* **1999**, *35*, 347–360. [CrossRef]
10. Katayama, I.; Abe, N.; Okazaki, K.; Hatakeyama, K.; Akamatsu, Y.; Michibayashi, K.; Godard, M.; Kelemen, P. Crack Geometry of Serpentinized Peridotites Inferred from Onboard Ultrasonic Data from the Oman Drilling Project. *Tectonophysics* **2021**, *814*, 228978. [CrossRef]
11. Shirole, D.; Hedayat, A.; Walton, G. Damage Monitoring in Rock Specimens with Pre-Existing Flaws by Non-Linear Ultrasonic Waves and Digital Image Correlation. *Int. J. Rock Mech. Min. Sci.* **2021**, *142*, 104758. [CrossRef]
12. Liu, W.; Wang, G.; Han, D.; Xu, H.; Chu, X. Accurate Characterization of Coal Pore and Fissure Structure Based on CT 3D Reconstruction and NMR. *J. Nat. Gas Sci. Eng.* **2021**, *96*, 104242. [CrossRef]
13. Wang, X.; Pan, J.; Wang, K.; Ge, T.; Wei, J.; Wu, W. Characterizing the Shape, Size, and Distribution Heterogeneity of Pore-Fractures in High Rank Coal Based on X-Ray CT Image Analysis and Mercury Intrusion Porosimetry. *Fuel* **2020**, *282*, 118754. [CrossRef]
14. Zhang, S.; Yan, J.; Cai, J.; Zhu, X.; Hu, Q.; Wang, M.; Geng, B.; Zhong, G. Fracture Characteristics and Logging Identification of Lacustrine Shale in the Jiyang Depression, Bohai Bay Basin, Eastern China. *Mar. Pet. Geol.* **2021**, *132*, 105192. [CrossRef]
15. Tabasi, S.; Soltani Tehrani, P.; Rajabi, M.; Wood, D.A.; Davoodi, S.; Ghorbani, H.; Mohamadian, N.; Ahmadi Alvar, M. Optimized Machine Learning Models for Natural Fractures Prediction Using Conventional Well Logs. *Fuel* **2022**, *326*, 124952. [CrossRef]
16. Lai, J.; Wang, G.; Fan, Z.; Wang, Z.; Chen, J.; Zhou, Z.; Wang, S.; Xiao, C. Fracture Detection in Oil-Based Drilling Mud Using a Combination of Borehole Image and Sonic Logs. *Mar. Pet. Geol.* **2017**, *84*, 195–214. [CrossRef]
17. Li, H.; Zhao, X.; Dai, B.; Huang, Z.; Zhu, Q. Study on the Evolution and Prediction of Fracture Depth of Surrounding Rock in Deep Mining Roadway Based on Numerical Analysis and Borehole Detection. *Front. Earth Sci.* **2022**, *10*, 1024240. [CrossRef]
18. Rozycki, A.; Ruiz Fonticiella, J.M.; Cuadra, A. Detection and Evaluation of Horizontal Fractures in Earth Dams Using the Self-Potential Method. *Eng. Geol.* **2006**, *82*, 145–153. [CrossRef]
19. Li, S.; Gu, X.; Xu, X.; Xu, D.; Zhang, T.; Liu, Z.; Dong, Q. Detection of Concealed Cracks from Ground Penetrating Radar Images Based on Deep Learning Algorithm. *Constr. Build. Mater.* **2021**, *273*, 121949. [CrossRef]
20. Talley, J.; Baker, G.S.; Becker, M.W.; Beyrle, N. Four Dimensional Mapping of Tracer Channelization in Subhorizontal Bedrock Fractures Using Surface Ground Penetrating Radar. *Geophys. Res. Lett.* **2005**, *32*, L04401. [CrossRef]
21. Eskandari Torbaghan, M.; Li, W.; Metje, N.; Burrow, M.; Chapman, D.N.; Rogers, C.D.F. Automated Detection of Cracks in Roads Using Ground Penetrating Radar. *J. Appl. Geophys.* **2020**, *179*, 104118. [CrossRef]
22. Dorn, C.; Linde, N.; Le Borgne, T.; Bour, O.; Klepikova, M. Inferring Transport Characteristics in a Fractured Rock Aquifer by Combining Single-Hole Ground-Penetrating Radar Reflection Monitoring and Tracer Test Data. *Water Resour. Res.* **2012**, *48*, W11521. [CrossRef]
23. Solla, M.; Lagüela, S.; González-Jorge, H.; Arias, P. Approach to Identify Cracking in Asphalt Pavement Using GPR and Infrared Thermographic Methods: Preliminary Findings. *Ndt E Int.* **2014**, *62*, 55–65. [CrossRef]
24. Tang, J.; Zhang, C.; Xin, Y. A Fracture Evaluation by Acoustic Logging Technology in Oil-Based Mud: A Case from Tight Sandstone Reservoirs in Keshen Area of Kuqa Depression, Tarim Basin, NW China. *Pet. Explor. Dev.* **2017**, *44*, 418–427. [CrossRef]
25. Tokhmchi, B.; Memarian, H.; Rezaee, M.R. Estimation of the Fracture Density in Fractured Zones Using Petrophysical Logs. *J. Pet. Sci. Eng.* **2010**, *72*, 206–213. [CrossRef]
26. Dias, L.O.; Bom, C.R.; Faria, E.L.; Valentín, M.B.; Correia, M.D.; de Albuquerque, M.P.; de Albuquerque, M.P.; Coelho, J.M. Automatic Detection of Fractures and Breakouts Patterns in Acoustic Borehole Image Logs Using Fast-Region Convolutional Neural Networks. *J. Pet. Sci. Eng.* **2020**, *191*, 107099. [CrossRef]
27. Leal, J.A.; Ochoa, L.H.; Garcia, J.A. Identification of Natural Fractures Using Resistive Image Logs, Fractal Dimension and Support Vector Machines. *Ing. Investig.* **2016**, *36*, 125–132. [CrossRef]
28. Lopes, J.A.G.; Medeiros, W.E.; Oliveira, J.G.; Santana, F.L.; Araújo, R.E.B.; La Bruna, V.; Xavier, M.M.; Bezerra, F.H.R. Three-Dimensional Characterization of Karstic Dissolution Zones, Fracture Networks, and Lithostratigraphic Interfaces Using GPR Cubes, Core Logs, and Petrophysics: Implications for Thief Zones Development in Carbonate Reservoirs. *Mar. Pet. Geol.* **2023**, *150*, 106126. [CrossRef]
29. Tokhmechi, B.; Memarian, H.; Rasouli, V.; Noubari, H.A.; Moshiri, B. Fracture Detection from Water Saturation Log Data Using a Fourier–Wavelet Approach. *J. Pet. Sci. Eng.* **2009**, *69*, 129–138. [CrossRef]
30. Lau, J.S.O.; Auger, L.F.; Bisson, J.G. Subsurface Fracture Surveys Using a Borehole Television Camera and Acoustic Televiewer. *Can. Geotech. J.* **1987**, *24*, 499–508. [CrossRef]
31. Li, S.J.; Feng, X.-T.; Wang, C.Y.; Hudson, J.A. ISRM Suggested Method for Rock Fractures Observations Using a Borehole Digital Optical Televiewer. *Rock Mech. Rock Eng.* **2013**, *46*, 635–644. [CrossRef]
32. Capineri, L.; Falorni, P.; Borgioli, G.; Bulletti, A.; Valentini, S.; Ivashov, S.; Zhuravlev, A.; Razevig, V.; Vasiliev, I.; Paradiso, M.; et al. Application of the RASCAN Holographic Radar to Cultural Heritage Inspections. *Archaeol. Prospect.* **2009**, *16*, 218–230. [CrossRef]
33. Hœrlé, S.; Huneau, F.; Salomon, A.; Denis, A. Using the Ground-Penetrating Radar to Assess the Conservation Condition of Rock-Art Sites. *Comptes Rendus Geosci.* **2007**, *339*, 536–544. [CrossRef]

34. Masini, N.; Nuzzo, L.; Rizzo, E. GPR Investigations for the Study and the Restoration of the Rose Window of Troia Cathedral (Southern Italy). *Near Surf. Geophys.* **2007**, *5*, 287–300. [CrossRef]
35. Catapano, I.; Gennarelli, G.; Ludeno, G.; Soldovieri, F. Applying Ground-Penetrating Radar and Microwave Tomography Data Processing in Cultural Heritage: State of the Art and Future Trends. *IEEE Signal Process. Mag.* **2019**, *36*, 53–61. [CrossRef]
36. Cripps, A.C.; McCann, D.M. The Use of the Natural Gamma Log in Engineering Geological Investigations. *Eng. Geol.* **2000**, *55*, 313–324. [CrossRef]
37. O'Neal, M.L.; McGeary, S. Late Quaternary Stratigraphy and Sea-Level History of the Northern Delaware Bay Margin, Southern New Jersey, USA: A Ground Penetrating Radar Analysis of Composite Quaternary Coastal Terraces. *Quat. Sci. Rev.* **2002**, *21*, 929–946. [CrossRef]
38. Hyndman, R.D.; Yuan, T.; Moran, K. The Concentration of Deep Sea Gas Hydrates from Downhole Electrical Resistivity Logs and Laboratory Data. *Earth Planet. Sci. Lett.* **1999**, *172*, 167–177. [CrossRef]
39. Liu, J.-J.; Liu, J.-C. Integrating Deep Learning and Logging Data Analytics for Lithofacies Classification and 3D Modeling of Tight Sandstone Reservoirs. *Geosci. Front.* **2022**, *13*, 101311. [CrossRef]
40. Guo, H.-S.; Feng, X.-T.; Li, S.-J.; Yang, C.-X.; Yao, Z.-B. Evaluation of the Integrity of Deep Rock Masses Using Results of Digital Borehole Televiewers. *Rock Mech. Rock Eng.* **2017**, *50*, 1371–1382. [CrossRef]